



RESEARCH ARTICLE

10.1002/2016JD025221

Key Points:

- mineral dust detection and source identification
- enhancement of RGB satellite imagery
- southern African dust activity

Correspondence to:

J. E. Murray,
j.murray@imperial.ac.uk

Citation:

Murray, J. E., H. E. Brindley, R. G. Bryant, J. E. Russell, K. F. Jenkins, and R. Washington (2016), Enhancing weak transient signals in SEVIRI false color imagery: Application to dust source detection in southern Africa, *J. Geophys. Res. Atmos.*, 121, doi:10.1002/2016JD025221.

Received 12 APR 2016

Accepted 14 AUG 2016

Accepted article online 17 AUG 2016

Enhancing weak transient signals in SEVIRI false color imagery: Application to dust source detection in southern Africa

J. E. Murray¹, H. E. Brindley¹, R. G. Bryant², J. E. Russell¹, K. F. Jenkins³, and R. Washington⁴

¹Space and Atmospheric Physics Group, Imperial College London, London, UK, ²Department of Geography, University of Sheffield, Sheffield, UK, ³Rutherford Appleton Laboratory, Didcot, UK, ⁴School of Geography and the Environment, University of Oxford, Oxford, UK

Abstract A method is described to significantly enhance the signature of dust events using observations from the Spinning Enhanced Visible and InfraRed Imager (SEVIRI). The approach involves the derivation of a composite clear-sky signal for selected channels on an individual time step and pixel basis. These composite signals are subtracted from each observation in the relevant channels to enhance weak transient signals associated with either (a) low levels of dust emission or (b) dust emissions with high salt or low quartz content. Different channel combinations, of the differenced data from the steps above, are then rendered in false color imagery for the purpose of improved identification of dust source locations and activity. We have applied this clear-sky difference (CSD) algorithm over three (globally significant) source regions in southern Africa: the Makgadikgadi Basin, Etosha Pan, and the Namibian and western South African coast. Case study analyses indicate three notable advantages associated with the CSD approach over established image rendering methods: (i) an improved ability to detect dust plumes, (ii) the observation of source activation earlier in the diurnal cycle, and (iii) an improved ability to resolve and pinpoint dust plume source locations.

1. Introduction

To better understand the processes governing the availability and entrainment of dust (mineral aerosols) into the atmosphere, dust sources and their associated activation patterns must be identified [Bryant, 2013]. A wide range of approaches have been developed utilizing observations from a variety of different satellite sensors to achieve this aim. Global maps of source regions and their relative strengths have been derived from instruments in low Earth orbit (LEO) such as the Total Ozone Mapping Spectrometer [Prospero *et al.*, 2002] and the Moderate Resolution Imaging Spectrometer (MODIS) [Ginoux *et al.*, 2012]. Given the spatial resolution, imagery from instruments such as MODIS can also be used to improve our knowledge of precise source locations [e.g., Baddock *et al.*, 2009; Vickery *et al.*, 2013, hereafter V2013]. However, for these LEO instruments the information available is restricted to the satellite overpass times. Dust emission from a specific source typically lasts of the order of hours or less, and many sources exhibit preferential times of emission within the daily cycle linked to the near surface wind regime [e.g., Allen *et al.*, 2015; Schepanski *et al.*, 2009]. Hence, LEO satellite overpass times may either not be coincident with active dust emission from a given source or alternatively may miss the precise start of the emission process. Indeed, Baddock *et al.* [2009] and Schepanski *et al.* [2012] highlight significant spatial and temporal limitations in the effectiveness of a variety of different detection algorithms using MODIS and other sensors. Hence, at a regional scale, some of the more successful approaches used to characterize the activity of different sources derive from high temporal resolution data available from instruments in geostationary orbit. For example, the widely used red-green-blue (RGB) dust rendering scheme developed by Lensky and Rosenfeld [2008, hereafter LR2008] makes use of selected thermal channels measured by the Spinning Enhanced Visible and InfraRed Imager (SEVIRI), the imager on board the Meteosat Second Generation series of geostationary satellites [Schmetz *et al.*, 2002], to contrast the brightness temperature signal between surface, cloud, and dust in a false color rendering scheme in which dust appears magenta. This scheme has provided the basis for numerous studies of northern African dust sources and factors governing their activation [e.g., Schepanski *et al.*, 2007, 2009, 2012; Ashpole and Washington, 2013], with the 15 min time resolution of the SEVIRI imagery proving an invaluable aid to tracking individual events. There are advantages to be gained from both the high spatial resolution observations from LEO and the high temporal resolution offered from geostationary orbit (V2013). The first enables fine-scale identification of the active source locations, but limited information of the evolution of

©2016. The Authors.

This is an open access article under the terms of the Creative Commons Attribution License, which permits use, distribution and reproduction in any medium, provided the original work is properly cited.

dust events, offered from geostationary orbit, required to link dust entrainment processes to the prevailing atmospheric and surface conditions [Bryant, 2003; Bryant *et al.*, 2007].

The LR2008 RGB dust rendering scheme principally relies on the thermal contrast between the land surface and dust, which, either in the early stages of an event when the dust is yet to be entrained to higher atmospheric layers or when the optical depth of an event is low, may be small. Furthermore, the precise coloring produced by the scheme is affected by the spectral surface emissivity, the optical properties of the dust itself, and the atmospheric water vapor burden. Hence, dust identification can be confounded by the presence of a near-surface temperature inversion, high atmospheric moisture content, changes in the chemical composition and size of the dust particles, and the surface properties of vegetation or certain geological features [Brindley *et al.*, 2012; Banks and Brindley, 2013].

Clearly then, while the high temporal resolution offered by SEVIRI is particularly beneficial in studies of short-lived dust events, there are limitations associated with the existing RGB dust rendering (a fact further emphasized by Vickery *et al.* [2013]), and it is therefore worth improving geostationary imagery of dust. With these factors in mind, the aim of this paper is to apply a relatively simple technique based on proven composite clear-sky schemes used in cloud property retrieval algorithms [e.g., Minnis and Harrison, 1984] to enhance the dust signal. Composite top of the atmosphere (TOA) clear-sky reflectance and thermal emission are subtracted from real-time channel values to remove the underlying component associated with the surface reflectance and emission. The residual component due to transient signals, including cloud and aerosol, can then be amplified to improve the contrast of the desired signals when rendered in false color imagery.

To provide a context for algorithm development in this paper, we review below two recent applications of this approach to dust detection. A similar background subtraction approach, the Robust Satellite Technique (RST), has been applied to natural and environmental hazard monitoring using remote sensing data [Tramutoli, 2007; Marchese *et al.*, 2010]. This technique is based on the derivation of an unperturbed measurement state and its standard deviation, derived for a given location and time. The unperturbed state is subtracted from the real-time measurement of the satellite and normalized by the standard deviation of the measurements making up the unperturbed state, yielding a local variation index known as ALICE (Absolute Local Index of Change of the Environment) [Tramutoli, 2007]. In formulation this is identical to the z or standard score [Cohen *et al.*, 2003]. The ALICE value for locations of interest can be monitored in real time for statistically significant deviation from the normal. This technique has been applied successfully to monitoring of volcanic activity [e.g., Marchese *et al.*, 2010]. Workers have subsequently extended this technique to dust detection through the use of RST-DUST applied to geostationary remote sensor data [Tramutoli *et al.*, 2010]. For example, Tramutoli *et al.* [2010] has applied RST-DUST to data acquired from the Japanese Advanced Meteorological Imager (JAMI) [Puschell *et al.*, 2006] on board the Japanese Multifunctional Transport Satellite (MTSAT-1R) [Puschell *et al.*, 2002]. ALICE indexes were calculated for the brightness temperature difference between the 11 μm and 12 μm JAMI channels. The reference field for this study was derived from 4 years of satellite data (120 days), but the underlying methodology behind selection of the clear-sky observation making up the reference is unclear. In addition, the ALICE index thresholds applied to flag dust laden pixels are not provided, making assessment of the sensitivity of this approach difficult. It is clear that this initial case study for RST-DUST was aimed at characterizing and monitoring an evolved dust cloud some days after the initial uplift. Importantly, our approach differs from this RST-DUST test case in two key ways: (i) we aim to isolate dust emission sites and entrainment timings at a time when thermal contrast between the dust and surface is at its lowest and (ii) where RST uses the standard deviation to normalize the variance from the average state we render the variance from the average state, selected from a 21 day window, as an RGB image using a fixed gain in place of the standard deviation.

Miller [2014] describes a comparable approach to enhance atmospheric signals in satellite channel radiances by subtracting the contribution of the underlying surface. Similar to our approach, Miller [2014] describes the combination and rendering of these enhanced channel signals as false color images, thus improving the contrast between, for instance, dust plumes, clouds, and the land surface. More recently, this scheme has formed the basis for the Dynamic Enhancement Background Reduction Algorithm (Miller, private communication, 2016). Here instead of deriving a clear-sky estimate from the satellite sensor of interest, Miller proposes the use of auxiliary surface emissivity and surface temperature data. The emissivity and temperature information is used to estimate what the clear-sky measurement values would be for preselected dust detection tests for

Table 1. SEVIRI Planck Function Coefficients for Selected Thermal Channels [Tjemkes, 2005]

Channel No.	ϑ (μm)	a	b
04	3.9	0.9959	3.471
07	8.7	0.9996	0.181
09	10.8	0.9983	0.627
10	12.0	0.9988	0.397

each pixel. These clear-sky estimates can then be used to either reduce false flagging in dust detection algorithms or to set scaling factors for dust enhancement in false color imagery. However, in the case of relatively weak dust signals, such as those highlighted here, other

factors besides surface conditions can confound dust detection. For example, day-to-day variations in atmospheric water vapor amount and the sporadic presence of smoke haze need to be considered as both affect the thermal contrast and can mask the signal from dust plumes (V2013).

It is important to note, therefore, that while our approach could be used for the detection of dust in a wide range of environmental regions, here we apply and tune it to southern Africa focusing particularly on the key dust source regions previously identified by V2013. In this location it is expected to offer a significant advantage over the LR2008 RGB dust scheme and the CDS approaches of Miller [2014] and Tramutoli *et al.* [2010]. This effort is part of a wider research program, the ongoing Dust Observations for Models project (DO4Models), aimed at improving dust emission schemes in regional climate models and comprising scientists from the UK and South Africa [e.g., Haustein *et al.*, 2015]. Sources in southern Africa are potentially important in terms of their effects on regional terrestrial, oceanic, and polar biogeochemical cycles as well as in the context of regional weather and climate prediction [e.g., Tummon *et al.*, 2010; Zhang *et al.*, 2015]. Indeed, recent research suggests that the region may emit substantially more dust in the future under specific climate change scenarios [e.g., Bhattachan *et al.*, 2012, 2015].

Our research is presented in the following three sections of this paper. In section 2 we briefly discuss how the temporal behavior of SEVIRI shortwave channel reflectance has previously been used in TOA clear-sky algorithms. We then introduce the measurements employed in this study and outline the scheme used for our estimates of TOA clear-sky reflectance and brightness temperature before showing how these clear-sky estimates can be combined with selected channel combinations to enhance transient dust signals in false color RGB imagery. In section 3 we apply the technique to selected dust events originating from key source regions in southern Africa to illustrate the particular advantages of our method. We then show how these benefits are more generally realized by applying the scheme to 4 years of SEVIRI observations over southern Africa. Finally, in section 4 we draw together our conclusions from this study including a discussion concerning the general applicability of the detection scheme.

2. DO4Models Dust Identification Scheme (DO4-DIS)

2.1. Data

In this study we use observations from the SEVIRI instrument on Meteosat-9, located above the equator and Greenwich meridian. SEVIRI is composed of 11 narrowband channels centered on 0.6, 0.8, 1.6, 3.9, 6.2, 7.3, 8.7, 9.7, 10.8, 12.0, and 13.4 μm with a ground resolution of 3 km at nadir and a single high spatial resolution channel with 1 km nadir resolution, covering the visible spectral region. LR2008 outline the process of conversion of the raw counts from these channels to brightness temperature for the thermal channels and solar reflectance for channels 0.6–1.6 μm . For clarity we repeat the process here for the channels used in this study. The relationship between channel count and spectral radiance, B ($\text{mW m}^{-2}\text{sr}^{-1} (\text{cm}^{-1})^{-1}$), is given by

$$B_\lambda = \text{offset}_\lambda + \text{gain}_\lambda \cdot \text{count}_\lambda$$

where the offsets and gains, located in the raw data header, are channel dependent.

For the thermal channels the variable used in the rendering scheme is brightness temperature, T_B , which is retrieved from radiance using the inverted Planck function,

$$T_B = \frac{c_2 \nu}{\ln \left\{ \frac{c_1 \nu^3}{B_\nu} + 1 \right\}} \tag{1}$$

$$T_B = \left(\frac{c_2 \nu}{\ln \left\{ \frac{c_1 \nu^3}{B_\nu} + 1 \right\}} - b \right) / a \tag{2}$$

where ν is the channel central wave number (cm^{-1}), $c_1 = 1.19104 \times 10^{-8} \text{ W m}^{-2} \text{ sr}^{-1} (\text{cm}^{-1})^{-1}$ and $c_2 = 1.43877 \text{ K} (\text{cm}^{-1})^{-1}$. In our work, equation (1) is applicable to SEVIRI data received before 5 May 2008, equation (2) is applicable to all files from this date, and a and b are channel-dependent constants given in Table 1.

The solar reflectance, R_{λ} , is given by

$$R_{\lambda} = \frac{B_{\lambda}}{\mu_0 F_0(\lambda)} \quad (3)$$

where μ_0 is the cosine of the solar zenith angle and $F_0(\lambda)$ ($\text{mW m}^{-2} \text{ sr}^{-1} (\text{cm}^{-1})^{-1}$) the extraterrestrial solar flux, which in turn can be expressed as a function of the extraterrestrial solar flux at equinox, $\overline{F_0(\lambda)}$ and the Earth-Sun distance ESD (au)

$$F_0(\lambda) = \frac{\overline{F_0(\lambda)}}{\text{ESD}^2} \quad (4)$$

where $\overline{F_0(\lambda)} = 20.76, 23.30$ and 19.73 for the $0.6, 0.8,$ and $1.6 \mu\text{m}$ channels, respectively, and ESD is a function of the Julian day

$$\text{ESD}(\text{JD}) = 1 - 0.0167 \cos\left(\frac{2\pi(\text{JD} - 3)}{365}\right) \quad (5)$$

2.2. Clear-Sky Estimation

The use of regional clear-sky composites of TOA visible reflectance is routinely used to facilitate cloud detection [e.g., *Ipe et al.*, 2003; *Minnis and Harrison*, 1984; *Rossow and Garder*, 1993]. *Ipe et al.* [2003, hereafter I2003], are of particular relevance here as they describe an algorithm designed to obtain composite clear-sky TOA reflectance utilizing the temporal and spatial resolution available from Meteosat-7 imager channels. In order to minimize the spatial variation in reflectance associated with different underlying surface types and vegetation cover, I2003's clear-sky algorithm is applied at the individual pixel level. Given the additional assumption that the reflectance from vegetated surfaces remains relatively stable for a given time of day over restricted time periods of between 60 and 120 days, I2003 were able to represent the observed TOA reflectance of a pixel as a baseline representative of the mean clear-sky reflectance for that time of day and a variable high reflectance bias associated primarily with variations in cloudiness.

Here we take a similar approach to derive clear-sky composite reflectance images from observations made by SEVIRI on Meteosat-9. SEVIRI views a fixed scene, encompassing a region of approximately 60°S – 60°N and 60°W – 60°E , and full scans of the Earth's disk over this region are available every 15 min. The full scans of each of the 11 narrowband spectral channels are composed of 3712×3712 individual pixels. The field of view of the SEVIRI instrument combined with its high temporal and spatial sampling is well suited to the study of dust emission from southern Africa.

As shown by V2013 and also highlighted by *Prospero et al.* [2002], *Washington et al.* [2003], and *Ginoux et al.* [2012], dust events observed in southern Africa originate from three principal regions, the Makgadikgadi pans in Botswana [see also *Bryant et al.*, 2007], the Etosha pans in Namibia [see also *Bryant*, 2003], and the Western coasts of Namibia and South Africa [see also *Eckardt et al.*, 2001]. Figure 1 shows the southern African region we have isolated for the purposes of this study. To provide a first illustration of our methodology, in this section we focus on four pixels, one in each of four representative regions: the Makgadikgadi Basin (A), Etosha (B), the Kalahari Desert (C), which is included as representative of the underlying surface transited by entrained dust, and an ocean pixel off the Namibian coast (D).

Figures 2a–2d (left) and 3a–3d (left) show for each day of August and October 2010, respectively, the observed diurnal variation of the SEVIRI $0.6 \mu\text{m}$ channel reflectance at 60 min temporal resolution for the four pixels identified in Figure 1 from 0500 to 1600 UTC (encompassing sunlit hours). In principle, clear-sky reflectance composites could be derived from any of the three shortwave channels available from SEVIRI. The choice of the $0.6 \mu\text{m}$ channel over the $0.8 \mu\text{m}$ and $1.6 \mu\text{m}$ is consistent with previous clear-sky compositing studies [*Rossow and Garder*, 1993]. Over ocean under nonglint clear-sky conditions, reflectance, while always low, tends to reduce with increasing wavelength as one moves from the visible to the near-infrared regime, dropping to close to zero at $1.6 \mu\text{m}$. Over desert and vegetated land surfaces, in the absence of snow cover, clear-sky reflectances are typically higher and increase with increasing wavelength [*Matthews and Rossow*, 1987].

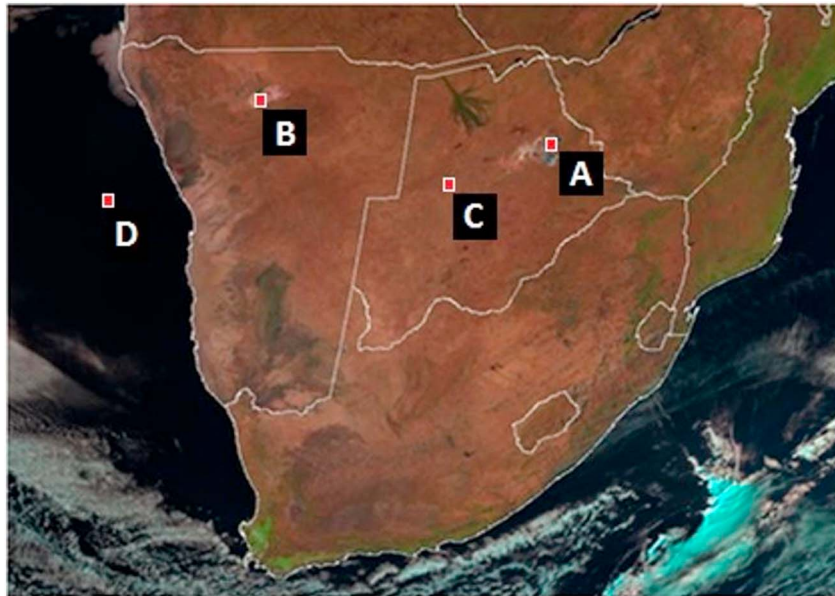


Figure 1. SEVIRI data showing the southern Africa region covered in this study at 13:15 UTC on 15 August 2010, rendered with the standard visible scheme of LR2008. The region comprises a 850 by 600 pixel subset of the full SEVIRI field of view corresponding to approximately 8–40°E by 16–35°S. Four pixels (A–D) used to investigate the variation of the 0.6 μm reflectance (see Figures 2–4) are marked in red.

Choosing the 0.6 μm channel thus provides a good compromise in terms of contrast between cloudy and clear-sky conditions over all surfaces likely to be encountered in the study region while ensuring that the signal always remains nonnegligible.

The clear-sky estimates are calculated for all seasons; however, we choose to display data from August and October because of the climatology of the region. August falls within the dry season when clear-sky conditions prevail over land as high-pressure systems dominate [e.g., Williams, 2010]. Vegetation can be senescent and the Etosha and Makgadikgadi pans are likely to be dry or drying [Bryant, 2003; Bryant *et al.*, 2007]. October is at the end of the dry season when the continental anticyclone is weakened by heating, and there is increased cloudiness [Piketh *et al.*, 2000, 2002]. The pans themselves have almost no vegetation, and variations seen in the surface reflectance are dominated by the surface moisture level. The dust season generally occurs between May and October, dust events tending to be associated with enhanced low-level easterlies [Eckardt *et al.*, 2001] although we note that records for the region have been derived from satellite observations which may struggle to detect dust in the presence of cloud.

For both August and October a baseline set of smooth reflectance curves can be picked out by eye relatively easily for each of the four locations. For example, in Figures 3a–3d (left) the reflectance baseline at the beginning of the month for Makgadikgadi is seen clearly in the dark blue lines and drops as the month progresses. As might be expected from the general rainfall climatology of the region, the land pixels show a relatively small amount of cloudiness in August (Figure 2) but substantially more in October (Figure 3), evidenced by the greater frequency of elevated reflectances in the latter month. Increased cloudiness in October is also seen over the ocean pixel although in this case there is also a significant amount of cloud cover earlier in the year.

One would expect at each UTC time, a trend in the baseline with changing solar zenith angle as the month progresses: this can be observed most clearly in the figures as an illumination time shift at dawn. There may also be a day-to-day variation in the baseline reflectance due to the presence of biomass-induced smoke haze which lowers the reflectance. Biomass burning in the southern African region can result in the presence of a general haze whose impact is dependent on the amount of burning, wind direction, and distance from source [Myhre *et al.*, 2003]. Close to source, strong absorption by intense smoke plumes can cause a relatively sharp, short-lived dip in reflectance, similar to the effect of cloud shadows, typically seen at elevated solar zenith angles. An example of the signal from the background biomass haze is given in section 2.4.

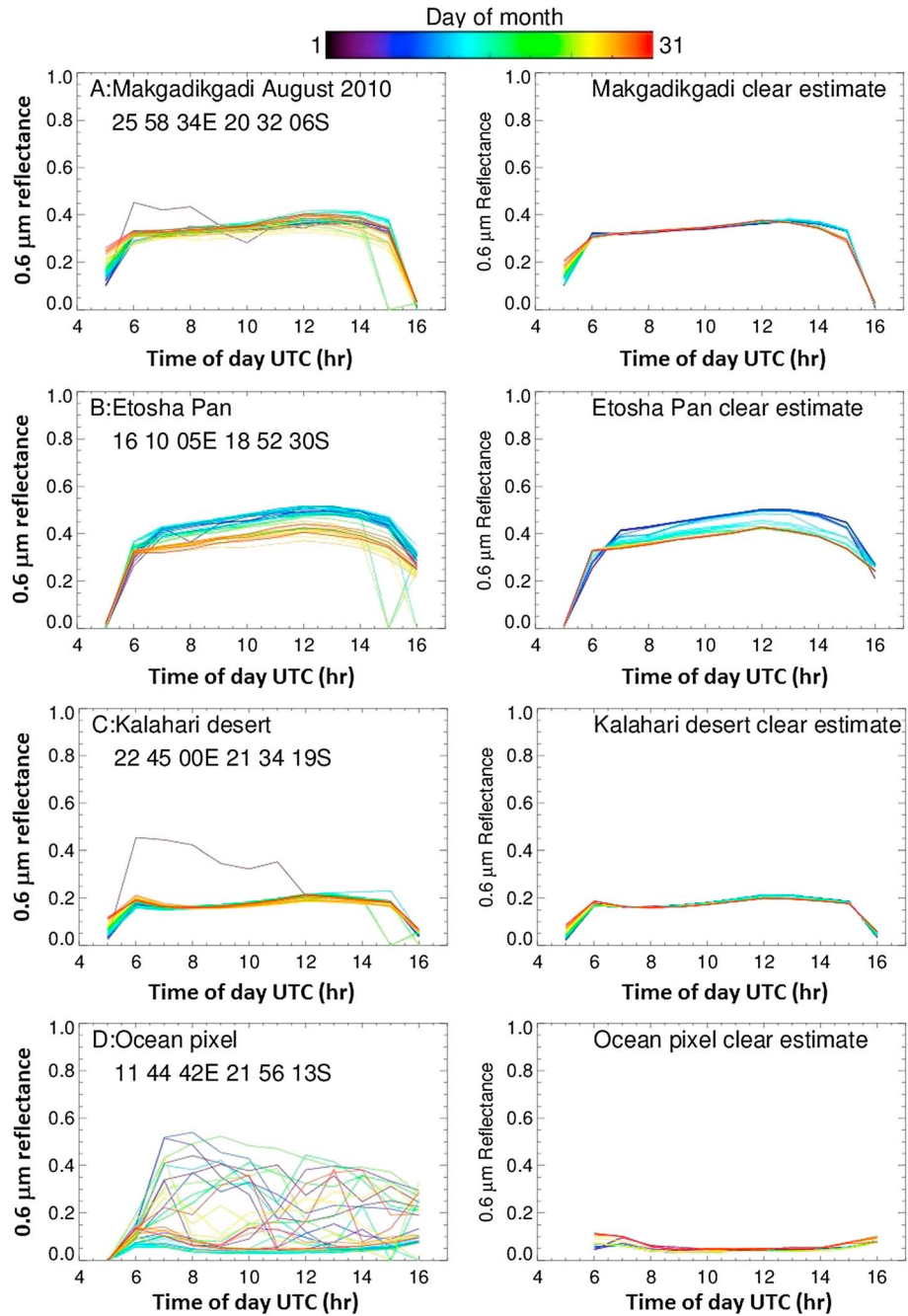


Figure 2. (a–d, left) Daytime diurnal variation in $0.6 \mu\text{m}$ reflectance for each day of August 2010 for the four pixels (A–D) highlighted in Figure 1. Each day of the month is represented by the line color. Dropouts to zero values indicate missing data. (right) The clear-sky estimation.

Given the modulation of the clear-sky reflectance by cloud and smoke plumes described above, we attempt to determine the clear-sky baseline in the following way for each individual pixel at hourly resolution between 0500 and 1600 UTC. For each day of interest, k , we employ a 21 day rolling window centered on k . Over this period, to mitigate for cloud-shadowing and smoke effects, we retain the third lowest reflectance value. We use this as a lower baseline and retain any reflectance values within the 21 day window that are within +12% of this value. In this way we essentially remove major cloud effects but allow for day-to-day fluctuations in nominally clear-sky conditions that may be a result of small changes in atmospheric and surface conditions, such as surface moisture levels. The composite “clear-sky” $0.6 \mu\text{m}$ reflectance for the given day is

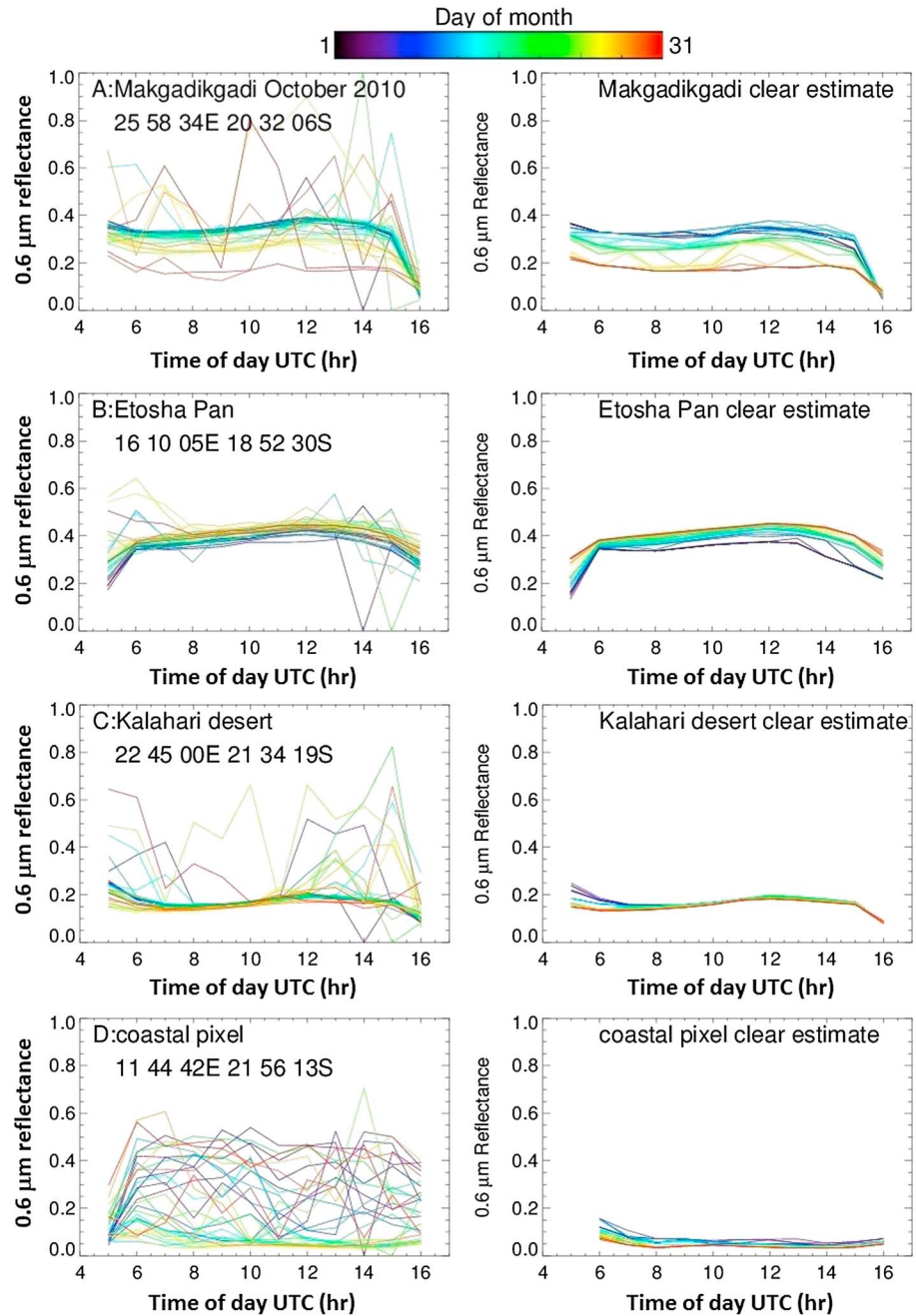


Figure 3. (a–d, left) Day-time diurnal variation in $0.6 \mu\text{m}$ reflectance for each day of October 2010 for the four pixels (A–D) highlighted in Figure 1. Each day of the month is represented by the line color. Dropouts to zero values indicate missing data. (right) The clear-sky estimation.

then obtained by averaging over the values that fall within this criterion. The choice of a 21 day window is driven by the wish to limit seasonal variations in the surface properties such as vegetation cover and surface moisture level while ensuring sufficient clear-sky observations at each time slot for the majority of pixels. The 12% reflectance mask was chosen from a visual inspection of a significant number of time series plots of the type shown in Figures 2 and 3. We apply a fixed reflectance discriminator independent of surface type, diurnal cycle, and season. When choosing this threshold, we found that values above 12% start to include significant weak cloud and fog signals over ocean and land pixels. For example Figure 3d shows a high level of cloud/fog reflectance variability over ocean which would contaminate the derived clear-sky average for high threshold values. Conversely, thresholds below 12% often have difficulty capturing real changes in

surface reflectance, as seen in Figure 3a. This rapid day-to-day change in the reflectance baseline is due to a change in the Makgadikgadi pan surface moisture levels through the month of October. Examples of the resultant clear-sky baselines are shown in Figures 2a–2d (right) and 3a–3d (right).

Equation (6) illustrates mathematically the procedure used where, for each pixel at each time step, $\rho_{0.6}^d$ is the 0.6 μm lower baseline reflectance (i.e., third lowest reflectance) over the 21 day rolling window, $\rho_{0.6}^k$ is the 0.6 μm reflectance on day k , m is the number of days used in the clear-sky average, and $\rho_{0.6}^{\text{csn}}$ is the derived clear-sky 0.6 μm reflectance on day n .

For days where $(\rho_{0.6}^d < \rho_{0.6}^k < 1.12 \times \rho_{0.6}^d)$

$$\left\{ \rho_{0.6}^{\text{csn}} = \left(\sum_{k=n-10}^{k=n+10} \rho_{0.6}^k \right) / m \right\} \quad (6)$$

We then use the day indices that were selected by this process to form the 0.6 μm clear-sky composite for each pixel at each time step to subsample reflectance and brightness temperatures in the other SEVIRI channels of interest in order to have a consistent set of clear-sky composite images.

2.3. Transient Enhancement in False Color Images

The clear-sky composites derived as described in section 2.2 are subsequently used to enhance the signal emanating from dust events. Over southern Africa these tend to be relatively weak and transient in nature compared to northern Africa [e.g., *Washington et al.*, 2003; *Ginoux et al.*, 2012]. Similar to LR2008, we use an RGB rendering approach but find that no one scheme is optimal for all cases and all times. Hence, we apply two different schemes, one which employs the solar reflectance and near-infrared channels on SEVIRI and one which uses thermal infrared information. In common with previous efforts [e.g., *Schepanski et al.*, 2007; *Vickery et al.*, 2013] interpretation of the resultant imagery requires an expert observer but, as we will show below, using both schemes in concert gives greater confidence in the discrimination of source activity.

In the shortwave channels, the red, green, and blue guns are assigned values given by the scaled difference between the channels of interest on the given day and time, and the corresponding clear-sky composite value (equation (7)), yielding clear-sky difference (CSD) images. The scaling factors are optimized through visual analysis carried out for a subset of images within the region identified in Figure 1 over the time span of interest from 05:00 to 1600 UTC. Analogous thermal images are rendered from brightness temperature measurements using a double difference approach, subtracting the clear-sky composite difference between selected channels from the corresponding instantaneous difference (equation (8)). The use of a reference brightness temperature difference at each time slot is designed to minimize the effects of variations in surface temperature and column water vapor on the derived signals, while the choice of channels is driven by previous dust detection work [e.g., *Wald et al.*, 1998; *Ackerman*, 1989, 1997]. As noted by *Wald et al.* [1998], the brightness temperature difference between the 10.8 and 8.7 μm channels will be sensitive to dust particle size, packing, and altitude. Generally, over silicate-dominated desert surfaces, smaller, elevated dust particles will have a higher emissivity than the underlying surface at 8.7 μm , while the converse is true at 10.8 μm . Under typical daytime conditions, the 12.0–10.8 μm split window difference will tend to become more positive in the presence of dust, behavior which is commonly used to distinguish dust from cloud [e.g., *Ackerman*, 1997]. Finally, the use of the 3.9 μm channel provides a reflectance component to the green gun which can be advantageous in detecting the presence of dust at elevated solar zenith angles [*Ackerman*, 1989].

$$\left\{ \begin{array}{l} \text{Red}_{8\text{bit}} = 15 * 255 * \left(\rho_{1.6\mu\text{m}} - \rho_{1.6\mu\text{m}}^{\text{csn}} \right) \\ \text{Green}_{8\text{bit}} = 15 * 255 * \left(\rho_{0.8\mu\text{m}} - \rho_{0.8\mu\text{m}}^{\text{csn}} \right) \\ \text{Blue}_{8\text{bit}} = 15 * 255 * \left(\rho_{0.6\mu\text{m}} - \rho_{0.6\mu\text{m}}^{\text{csn}} \right) \end{array} \right\} \quad (7)$$

$$\left\{ \begin{array}{l} \text{Red}_{8\text{bit}} = 0.5 * 255 * \left\{ \left(\text{BT}_{12.0\mu\text{m}} - \text{BT}_{10.8\mu\text{m}} \right) - \left(\text{BT}_{12.0\mu\text{m}}^{\text{csn}} - \text{BT}_{10.8\mu\text{m}}^{\text{csn}} \right) \right\} \\ \text{Green}_{8\text{bit}} = 0.25 * 255 * \left\{ \left(\text{BT}_{3.9\mu\text{m}} - \text{BT}_{10.8\mu\text{m}} \right) - \left(\text{BT}_{3.9\mu\text{m}}^{\text{csn}} - \text{BT}_{10.8\mu\text{m}}^{\text{csn}} \right) \right\} \\ \text{Blue}_{8\text{bit}} = 0.5 * 255 * \left\{ \left(\text{BT}_{8.7\mu\text{m}} - \text{BT}_{10.8\mu\text{m}} \right) - \left(\text{BT}_{8.7\mu\text{m}}^{\text{csn}} - \text{BT}_{10.8\mu\text{m}}^{\text{csn}} \right) \right\} \end{array} \right\} \quad (8)$$

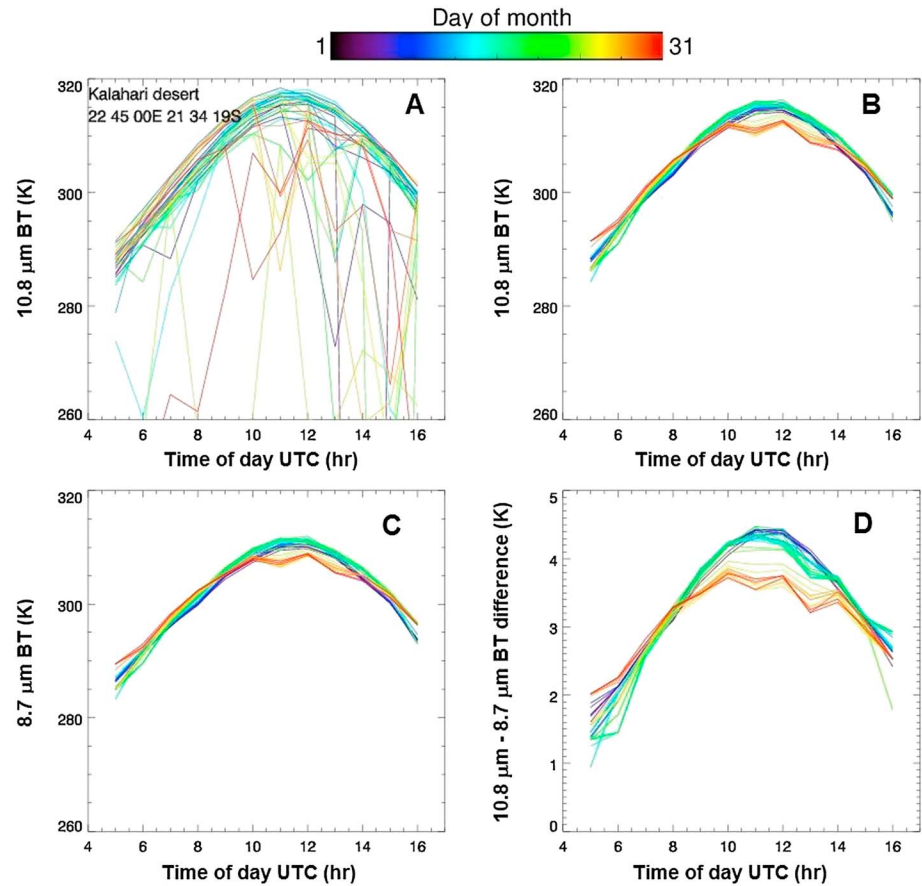


Figure 4. (a) SEVIRI 10.8 μm brightness temperature for the same pixel and period over the Kalahari desert as shown for the 0.6 μm reflectance in Figure 3c. (b and c) The estimated clear-sky signals for the 10.8 and 8.7 μm channels, respectively. (d) The 10.8 and 8.7 μm brightness temperature difference.

2.4. Some Examples of the Limitation Imposed by Natural Scene Variance on Image Enhancement

Figure 4 shows an example of the SEVIRI 10.8 μm brightness temperature measurements over the Kalahari, Figure 4a. At 10.8 μm atmospheric transmittance is high, and the signal is dominated by the surface temperature in the absence of cloud. Where cloud is present, we see sporadic drops in temperature dependent on cloud opacity and cloud top height. All other thermal channels used in our rendering scheme are similar in behavior and are therefore not shown. Figures 4b and 4c show the composite clear-sky 10.8 and 8.7 μm brightness temperatures. From this we see at certain times of the day, in this case at 11:00 and 13:00 UTC, averaging using equation (6) is underestimating the brightness temperature. In the thermal image rendering scheme we employ channel differencing, see equation (8), to minimize this effect. Figure 4d shows the brightness temperature difference for 10.8 and 8.7 μm , and although there is still an underestimation, this is a few tens of Kelvin, 0.1 K corresponds to 5% of the red and blue dynamic range and 2.5% of the green.

Figure 5 shows a rendered image for southern African from SEVIRI at 12:00 UTC on the 23 August 2010 (Julian day 235). Inset top right are plotted 12:00 UTC time series for SEVIRI 0.6 μm reflectance values between day 200 and 250 for two SEVIRI pixels marked A and B. Pixel A raw reflectance is in blue with the clear-sky estimate shown as green. There is a day-to-day variation in reflectance of about 0.01, which we attribute to variation in atmospheric transmittance, most likely smoke haze. Between days 228 and 230 there is a step down in the reflectance of about 0.04 lasting 10 to 15 days with the exception of day 235 where a sudden jump in reflectance is observed. Pixel B shows a similar behavior with the exception that on day 235 we see a drop in reflectance. On day 235 there was a CALIPSO overpass, track shown in green on image. To the left of Figure 5 is shown the CALIPSO aerosol optical depth, at 532 nm, with the latitude range set to match that of the image. This shows that on day 235 the aerosol optical depth was negligible over pixel A, while that over

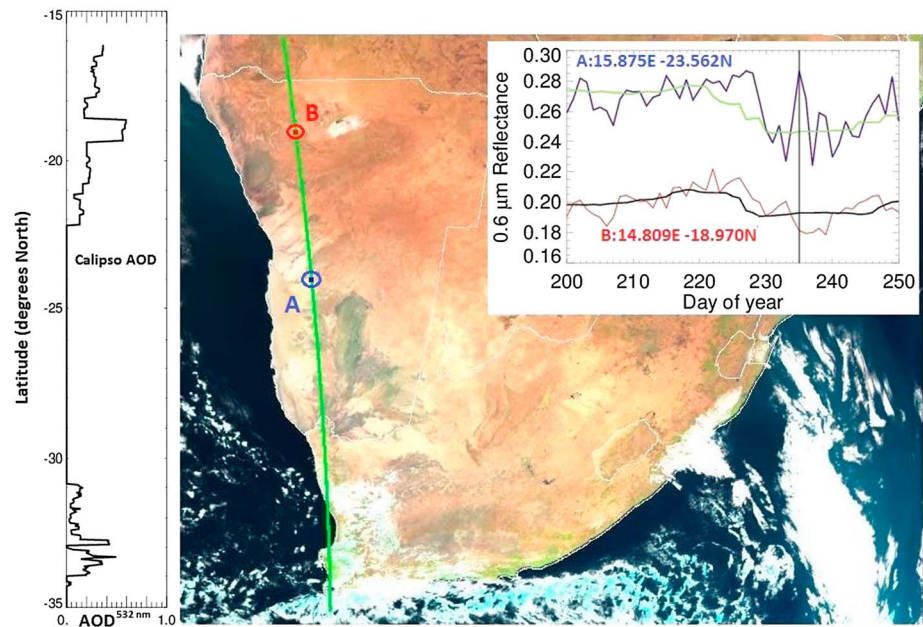


Figure 5. The southern African region as defined in Figure 1 for the 23 August 2010 (Julian day 235). Inset top right is the 12:00 UTC SEVIRI $0.6 \mu\text{m}$ reflectance time series for two pixels marked A and B and colored blue and red, respectively. The clear-sky reflectance estimate for A is shown in green and that for B is the curve in black. The vertical line at day 235 coincides with a CALIPSO overpass at 12:40 UTC. The CALIPSO aerosol optical depth for 532 nm channel is shown to the left with the graph latitude scale approximately match the image latitude range.

pixel B shows a high aerosol concentration. The CALIPSO classification for this aerosol is given primarily as biomass smoke and gives confidence in our assumption that the day-to-day variance in the observe reflectance is due to smoke haze variance. For efficient enhancement of dust signals we require the clear-sky estimate to follow reflectance variation in smoke haze, which it does reasonably well as seen between days 200–220 and 230–250. The day-to-day variance is smoothed out by our averaging window so we see a transition offset between days 220 and 230. A reflectance 0.01 corresponds to 15% of the dynamic color ranges of equation (7).

In the following section we consider specific examples of our rendering schemes as applied to dust emissions from the three primary source locations, Etosha, the Makgadikgadi Basin, and the western coast of southern Africa. Since the LR2008 RGB thermal dust imagery has been used in a number of studies to detect dust presence and sources, we also render the data according to their dust scheme. In addition, we also produce two further sets of false color imagery from the SEVIRI shortwave channels based on the work of LR2008. Over Etosha and Makgadikgadi we use the LR2008 standard visible RGB scheme. Plumes emerging from the coast over the ocean are better enhanced using the LR2008 stretched visible RGB rendering than the standard scheme and so we also show these for comparison for coastal scenes. While these two visible renderings struggle to identify source locations because of the lack of contrast between the airborne dust and underlying bright surface, they do aid overall interpretation, particularly for plumes which are advected away from the source over the ocean or darker vegetation. All the RGB images presented here employ 8 bit RGB rendering schemes with values running from 0 to 255. Any value less than zero is set to zero, and values greater than 255 are set to 255.

3. Dust Scheme Application

Although northern Africa represents the largest and most intense source region for dust, emissions are also observed globally in a range of quite different environmental contexts (e.g., semiarid and polar) [see e.g., Bryant, 2013] where emissions are more intermittent with an inherently low optical depth, and dust chemistry, atmospheric conditions, and landscape parameters (e.g., vegetation density) can vary significantly. Thus, despite the fact that it was not developed for use over nondesert surfaces, the LR2008 RGB dust scheme has also been employed to help inform a study of dust sources within southern Africa (V2013). V2013 is the

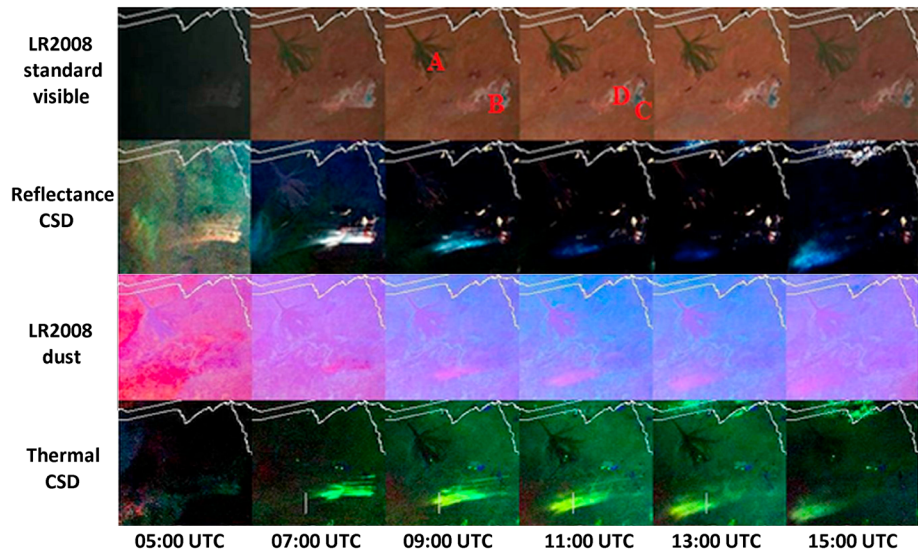


Figure 6. Rendered images over Botswana (Image location: upper left pixel: 17° 54S 21° 00E, lower right pixel: 21° 00S 26° 30E) highlighting the Makgadikgadi pan (B) and Okavango delta (A) at 2-hourly time steps from 05:00 to 15:00 UTC on 11 August 2010. (top row) LR2008 standard visible RGB. (second row) Reflectance CSD RGB as defined by equation (7). (third row) LR2008 “dust” RGB. (bottom row) Thermal CSD RGB as defined by equation (8).

most comprehensive study of dust plumes and sources over southern Africa to date. In this work the authors performed a visual inspection of MODIS and SEVIRI imagery from 2005 to 2008 and vastly improved the southern African dust source inventory from 10 to just over 100 locations. For MODIS the RGB images were rendered from three visible channels centered at 0.55, 0.645, and 0.69 μm , had a spatial resolution of 0.25 km, and were nominally available at the satellite overpass times of \sim 08:30 UTC (Terra) and \sim 13:30 UTC (Aqua) each day. These data were supplemented by daily SEVIRI LR2008 RGB dust images from 07:00, 10:00, and 13:00 UTC. Note that in practice, not all available slots were available for the whole 4 year period. V2013 found that dust emissions in southern Africa tend to be typically short-lived, early morning events. They identified three main emission regions: the Makgadikgadi basin, Etosha basin, and Namib coastal sources. In the case of the Namib coast the source types are varied (pans, ephemeral rivers, wetlands, and possibly mines), while both the Makgadikgadi and Etosha are classified as large pans (or Ephemeral Lakes) [Goudie and Viles, 2015; Bryant et al., 2007].

We now apply the rendering schemes outlined in section 2 to selected case studies, associated with the regions identified by V2013, in order to assess their relative performance. We note that a quantitative assessment of performance in the study region is problematic due to a lack of ground-truth observations. Conventional comparisons with retrieved aerosol optical depths from instruments in LEO (e.g., MODIS and Multiangle Imaging Spectroradiometer) can be compromised by assumptions concerning surface type in the retrieval algorithms (A. Sayer, personal communication, 2014) but more critically by the spatial resolution of the retrievals, the potential for aerosol mixtures to be contributing to the observed signal (e.g., biomass and dust) and/or the sparsity of collocations when a source is active.

In an attempt to circumvent these issues, for the studies selected here we have extracted 250 m resolution Terra MODIS level 1b data (MOD02QKM) and applied the rendering of equation (7) to channels 1 and 2 (0.645 and 0.858 μm , respectively), thus obtaining green-blue images. While this can only provide a snapshot view of the given dust events, it allows a comparison to be made with the equivalently timed, coarser spatial resolution SEVIRI dust imagery.

Conversion of the MODIS data to reflectance R_λ was performed following the procedure outlined in the MODIS level 1b product user’s guide [MODIS Characterisation Support Team, 2006].

$$R_\lambda = \text{Scale}_\lambda \cdot (S_{i_\lambda} - \text{offset}_\lambda) \tag{9}$$

where S_{i_λ} is an unsigned scaled integer value of 16 and the scale and offset values are obtained from the relevant data file. The MODIS clear-sky background reflectance needed to implement the approach of

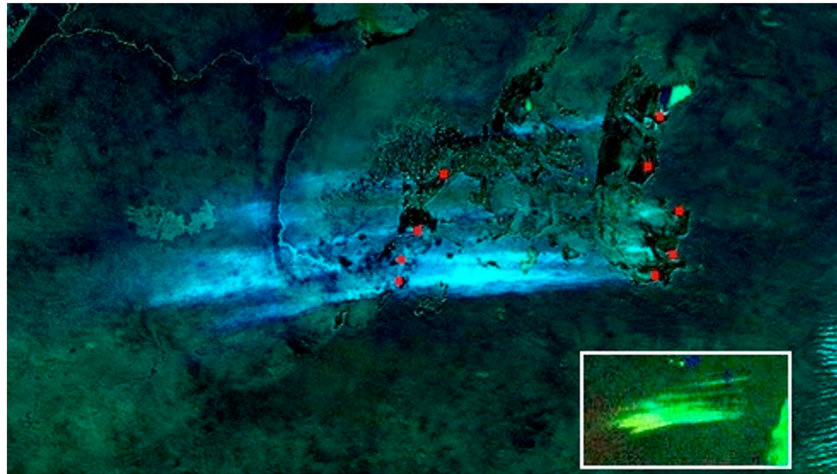


Figure 7. MODIS Terra green-blue rendered image over the Makgadikgadi region for 11 August 2010 at 08:05 UTC. The image is derived using equation (7) and MODIS channels 1 and 2 at 250 m resolution, where the subtracted “background” signal is from 08:15 UTC on 9 August 2010. The dust source locations identified from the SEVIRI CSD data are marked by red squares (see text for identification method). Inset is the SEVIRI CSD rendered image for 08:00 UTC.

equation (7) was selected by careful visual analysis of the MODIS level 1b images with the caveats that the overpass time of the clear-sky observations must have been within 30 min of the dust event observations and that there must have been no more than 3 days between the clear and dusty days.

3.1. Case Study I: The Makgadikgadi Pans, Botswana

Figure 6 shows a region of Botswana covering the Makgadikgadi Basin, (B) and Okavango delta, (A), on 11 August 2010. This day saw a large dust emission event from the Makgadikgadi in the form of several discrete dust plumes. Although the plumes can be discerned in the LR2008 RGB standard visible imagery, pinpointing their origin in these images against the highly reflective background of the pans is difficult. Difficulty in precise source detection is not surprising as the visible rendering of LR2008 is not designed to visualize dust. However, the origin of the active dust plumes becomes readily identifiable, to within a pixel (~ 4 km) in the CSD image at 05:00 UTC (second row). At 07:00 UTC two main emission regions of activation can clearly be seen, one in the central Makgadikgadi (indicated by D in the 11:00 UTC image for reference) and the other at the southern end of Sua pan (C).

Analyzing the imagery at higher temporal resolution (not shown) suggests that the plumes were active from before 05:00 UTC until shortly after 08:00 UTC, when the connection between the plume tail and source becomes detached. Exploiting the temporal information available in the SEVIRI imagery allows us to link dust emission to the key meteorological processes responsible for the dust uplift. Between 05:00 and 15:00 UTC there is an observable change in color of the plume in the reflectance CSD images that may be due to changes in the properties of the dust associated with source location, aging, or due to changes in illumination conditions and surface reflectance through the day [Baddock *et al.*, 2009]. Early in the day the plumes appear white, signifying higher reflectance in all three SEVIRI visible channels relative to the composite background and the likelihood of higher evaporate mineral and lower quartz content in the plume. The rate that the reflectance from the plume decreases with time is wavelength dependent with the $1.6 \mu\text{m}$ channel (red) reflectance dropping off most rapidly.

Thermal images for the same event are shown in Figure 6 (third and fourth rows). Significantly, RGBs produced using the LR2008 RGB dust scheme struggle to identify dust emission prior to 0700 UTC and even at this time much of the detail concerning precise source locations is lost. The plume becomes more obvious above the underlying surface in this scheme from 0900 UTC onward, before diurnal cooling of the surface reduces the thermal contrast between the plume and the surface resulting in a loss of dust discrimination by 1500 UTC. Turning to the thermal CSD images, at 0500 UTC there is a hint that dust emission is occurring although the signal is clearly much weaker than in the corresponding reflectance CSD image. However, by 0700 UTC dust emission is very evident, and individual source locations can be distinguished. By 09:00 UTC

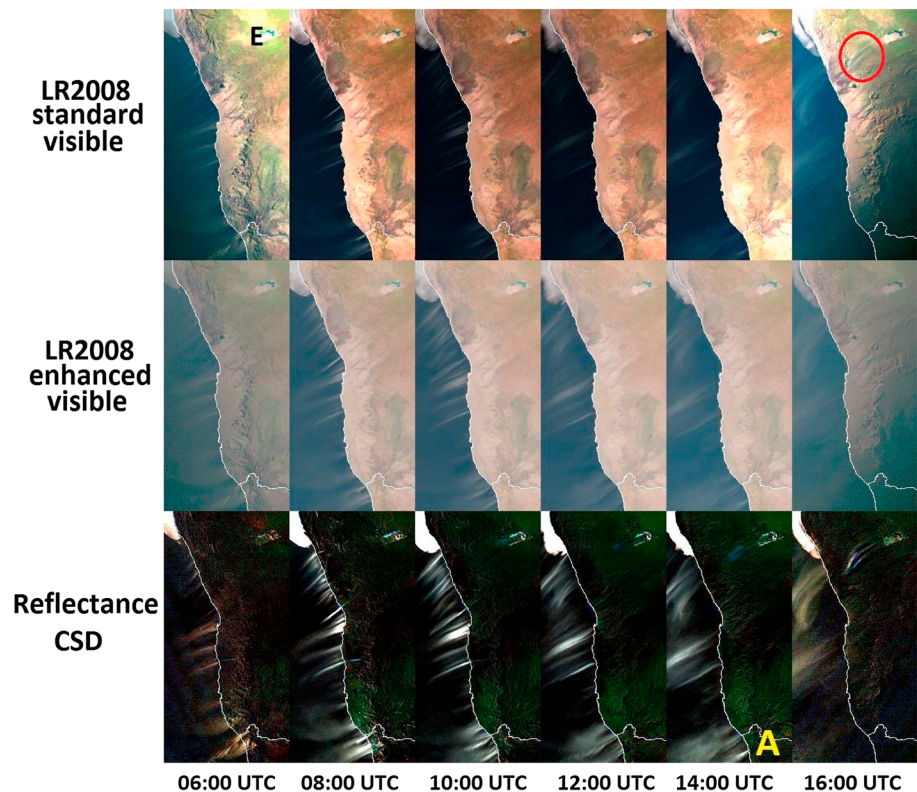


Figure 8. Rendered images (Image location: upper left pixel: 17° 00S 11° 23E, lower right pixel: 29° 15S 18° 17E) over the Namibian coast and Etosha pan region (E) at 2-hourly time steps from 06:00 to 16:00 UTC on 17 June 2010. (top row) LR2008 standard visible RGB, (middle row) LR2008 enhanced visible RGB, and (bottom row) standard reflectance CSD RGB.

the thermal CSD also clearly identifies weak plumes that are missed by the reflectance CSD. These thermal images also show much greater detail in plume location and extent relative to both the LR2008 visible rendering and the reflectance CSD between 09:00 UTC and 13:00 UTC. By 1500 UTC contrast between individual plumes is somewhat diminished although their presence is substantially easier to determine using either the reflectance or thermal CSD images compared to the LR2008 RGB dust rendering. In the presence of dust the thermal CSD scheme is dominated by scattering at $3.9\ \mu\text{m}$ which gives the dust plume its green color. From this example it is apparent that the reflectance and thermal CSD schemes offer complementary information. The reflectance CSD better captures dust source detail near sunrise, while the thermal CSD helps to highlight plume development through the morning and into the late afternoon.

To provide confidence in the inferences made above, Figure 7 shows a green-blue background subtracted image derived from MODIS Terra level 1b 250 m radiances for an overpass time of 08:05 UTC on 11 August 2010. Here the clear-sky background signal used was taken from the 08:15 UTC overpass 2 days prior to the dust event. The image clearly shows the presence of multiple plumes similar to those resolved by the SEVIRI CSD technique over the same period (Figure 6). Also shown in Figure 5 are estimated dust source locations (red squares), derived by animating the SEVIRI images and pinpointing the source pixel through a point and click graphical interface which returns the latitude and longitude of the highlighted pixel. While the snapshot MODIS data cannot be used to provide insight concerning dust event evolution, it is comforting to see that the source locations map very closely to the plumes identified in the higher spatial resolution imagery. The extent of each red square is the approximate size of a SEVIRI pixel.

3.2. Case Study II: The Namibian Coast and Etosha Pans

Figures 8 and 9 show images rendered from SEVIRI data taken on 17 June 2010. On this day large plumes of dust were observed off the Namibian and northwestern South African coast and Etosha Pan (marked E in Figure 8). Figure 8 (top row) shows LR2008 standard visible rendered images which just capture the dust

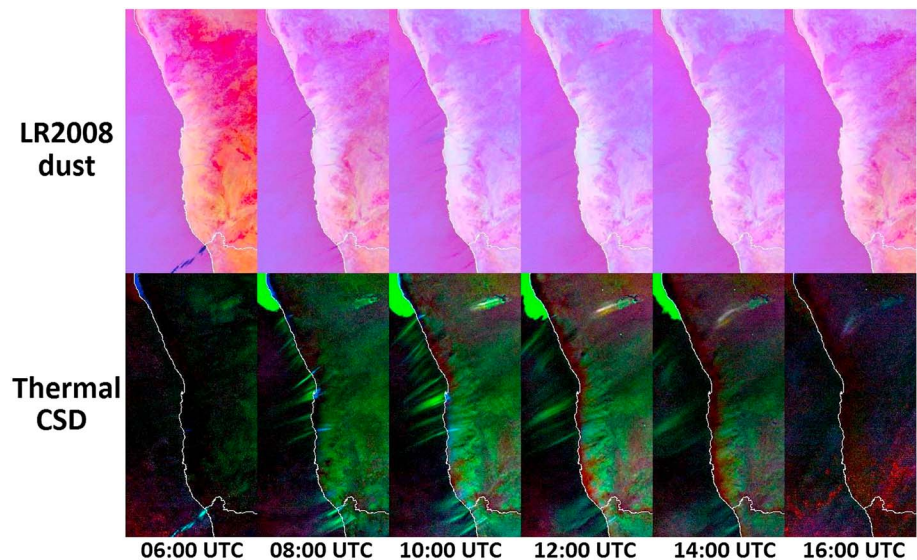


Figure 9. As Figure 8 but images rendered using (top row): LR2008 thermal dust rendering, and (bottom row) standard thermal CSD rendering.

plume, circled in red, from Etosha at 16:00 UTC. At this time the solar illumination angle of the plume is high, and the plumes are contrasted against their own shadows. Over ocean pixels the standard image does not capture the coastal plumes but not as clearly as the enhanced LR2008 visible images, shown in Figure 8 (middle row). The equivalent reflectance CSD images bring out the detail over the ocean more clearly and also, between 06:00 and 08:00 UTC, allows identification of some inland sources. Dust emission from Etosha Pan can be seen in the reflectance CSD renderings to start at around 10:00 UTC in the form of two distinct bluish plumes, but the contrast is relatively poor and does not easily allow identification of the precise sources of the plumes.

Both the Etosha sources and additional inland sources along the coast are seen in more detail in the LR2008 RGB dust and thermal CSD images (Figure 9). The inland sources are apparent, while they are actively emitting, and this gives information on the activation timing as well as precise source location. For example, on this day all Namibian sources cease emitting shortly after 10:00 UTC. In contrast, sources in the South African coastal region, the Uguchab, Orange and Holgat Rivers, are still emitting at 12:00 UTC. The Holgat also appears to intensify in emission at 14:00 UTC, marked A in Figure 8 (bottom row). In addition to the coastal dust events, the three dust plumes originating from Etosha are more obviously apparent in the thermal CSD rendering. The LR2008 RGB dust imagery does enable dust presence to be observed here, but it is difficult to resolve the individual plumes.

Figures 10a (09:35 UTC) and 10b (09:40 UTC) show background subtracted MODIS Terra green-blue images for this case study. Here MODIS data from the 19 June are used to derive the clear-sky background signal. Coastal plume crossings as identified from the SEVIRI CSD visible imagery are overplotted as red, while white squares indicate dust sources identified in an identical manner to those for Makgadikgadi. Typically, both show good agreement with the MODIS rendering. Some inland source locations are not identified by MODIS due to a mismatch between the source activation time and the Terra overpass. Conversely, the MODIS images show a level of detail and contrast that cannot be matched by SEVIRI due to the former's higher spatial resolution. This highlights that some plumes are missed by the CSD-SEVIRI approach, particularly along the southern Namibian/northern South African coast. However, there is clearly a marked improvement when using this technique compared to any of the LR2008 rendering approaches.

3.3. Relative Performance of SEVIRI Based Detection Schemes Over a Multiyear Period

In the previous examples we have shown how the CSD technique can improve our ability to observe dust activation, pinpoint dust sources, and detect weak dust events compared to the LR2008 renderings. The examples indicated advantages that could prove significant in building up a dust climatology for the various

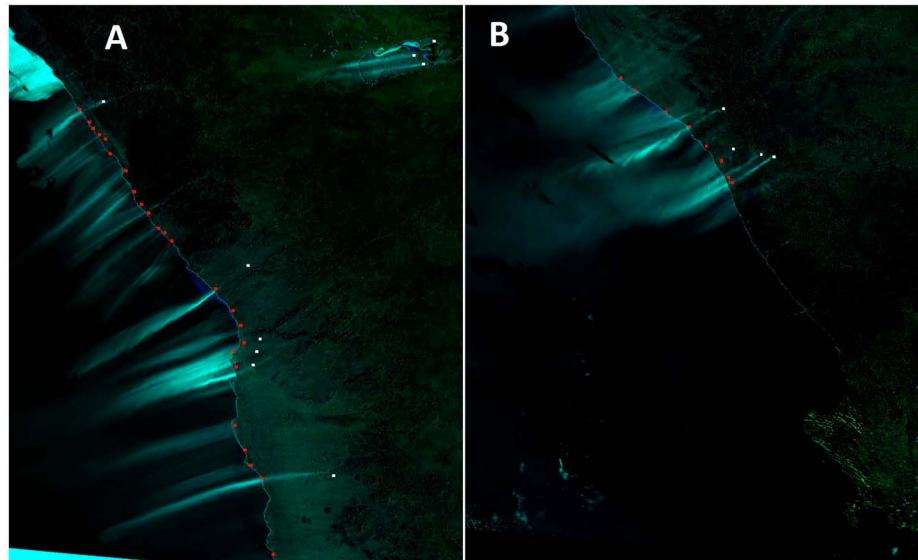


Figure 10. (a) As Figure 8 for MODIS Terra at 09:35 UTC on 17 June 2010. Red and white squares indicate dust plume coastal crossing points and inland source locations, respectively, as identified by SEVIRI CSD imagery. The MODIS Terra overpass at 09:25 UTC on 19 June 2010 was used to provide the clear-sky background signal. (b) As Figure 8 for MODIS Terra at 09:40 UTC on 17 June 2010. The MODIS 19 June 09:25 UTC overpass is used for the clear-sky background signal subtracted in this rendering.

source regions as a whole and for identifying timings of emission in order to unlock an understanding of the atmospheric processes responsible for the dust events. Case Study I highlighted how earlier detection of dust corresponding to the time of source activation was achieved with the CSD technique and also illustrated how multiple plumes could be distinguished with the CSD renderings. Case study II showed how the CSD technique improved the identification of dust over the ocean off the coast of southern Africa and provided an enhanced ability to observe the inland sources of these coastal plumes. To determine how consistent these advantages are over a wider range of conditions and evaluate the resulting difference in terms of the number of dust events recorded and their source locations, here we apply the CSD and LR2008 dust renderings to 4 years of SEVIRI observations focusing specifically on the Etosha and Makgadikgadi pans, and sources within the Namibian and southern African coastal region.

3.3.1. Time Series Comparison of CSD and LR2008 Retrievals

Thermal and reflectance CSD and LR2008 dust images were derived from hourly SEVIRI data between 05:00 UTC and 16:00 UTC inclusive for each day of the 4 years 2008 to 2011 and surveyed first to identify dust events and then to pinpoint source locations. For each event the period during which dust was visible in the CSD renderings and LR2008 dust imagery was recorded, and dust source locations were determined based first on the CSD imagery and then on the LR2008 dust imagery alone. For the purposes of this analysis we present the comparison in terms of the percentage of dust days and individual dust plumes identified by the LR2008 dust rendering compared to the CSD technique. This approach is chosen because based both on the case study results and an initial survey of the full record, we found that the CSD technique always detects dust when it is apparent in the LR2008 dust rendering but that the converse is not always true. Our analysis approach also means that the results presented are likely to show the ability of the LR2008 dust rendering to detect southern African dust events in its most favorable light. Weaker signals that may have been missed by an observer using just the LR2008 dust images may be more likely to be classified as dusty in this rendering once they have been identified using the CSD approach. We do however note that detection using either method involves a degree of subjectivity on the part of the observer: we plan to investigate the effects of this on the precise number of dust events detected and the overall climatology of the region in subsequent publications.

Figure 11a shows the percentage of dusty days identified in the LR2008 dust imagery compared to the number detected using the CSD approach subdivided by region and year. We define a dusty day as one in which a dust signal is seen at any point between 0500 and 1600 UTC in the relevant rendering over the specific

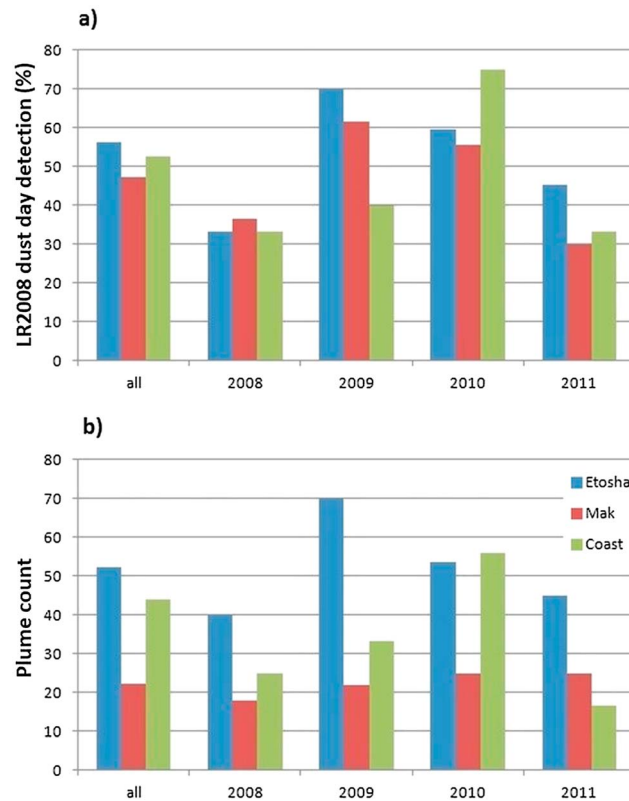


Figure 11. (a) Percentage of dusty days identified by the CSD method (all renderings) which show some discernible signal in the LR2008 dust imagery. (b) Number of individual plumes counted using the LR2008 dust imagery alone as a percentage of the plumes counted using the CSD techniques.

region. Hence, it is perfectly possible that more than one dust event may occur within a region on a particular day or that the CSD and LR2008 approaches may not highlight a particular dust event at the same time during the day. Averaged over the 4 years of the comparison, LR2008 dust imagery identifies about 50% of days which are classified by the CSD technique as exhibiting dust emission and this percentage is relatively consistent across all three study regions. However, resolved by year, this detection percentage is seen to vary significantly, with some additional variation between regions. This interannual variation appears to be at least in part a function of the frequency of dust emission days and the intensity of the individual plumes. For example, both techniques identify significantly more individual dust events and hence dusty days in 2010 compared to 2008 (not shown). However, the events that are present in 2008 tend to be weaker, and as expected from the previous section, the CSD approach is more successful at enhancing these signals. Hence, the percentage of these events identified by LR2008 dust imagery is somewhat reduced.

Figure 11b shows the number of distinct individual dust plumes counted on days observed to have dust emission using the LR2008 dust imagery as a percentage of the number of dust plumes counted using the CSD technique. Taken over 4 years, combining all regions, the LR2008 plume count is about 40% of the CSD plume count. This proportion does show a marked variation between the three dust source regions. Over Etosha the LR2008 dust imagery is able to capture around 50% of plumes identified by the CSD approach. The plume detection level drops a little for the coastal region and dramatically for the Makgadikgadi where the LR2008 plume count is 20% of the CSD count. The large disparity in plume count between LR2008 and the CSD approach for the Makgadikgadi is due to the improved resolution of the individual plumes and sources as seen in Figure 6. Dust emission from Etosha is typically seen as two plumes usually well resolved by both rendering techniques, and hence, dust days and plume counts are better matched. For the coast both techniques tend to resolve individual plumes equally well, here the slight disparity between dust days and plume count is mainly due to the improved detection of weaker signals.

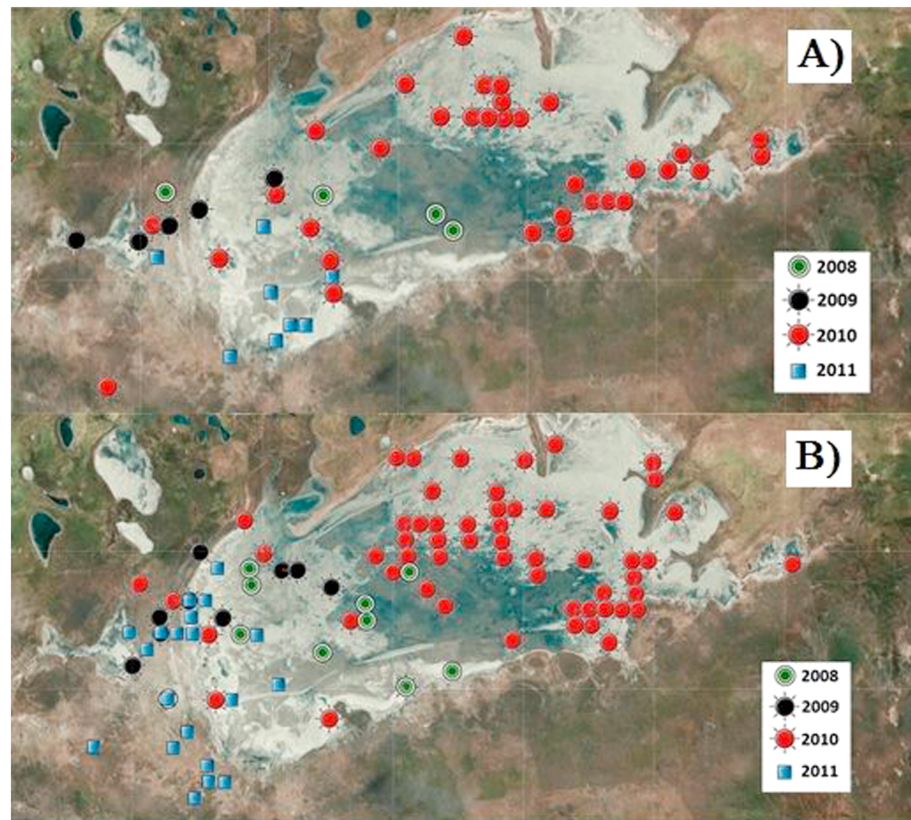


Figure 12. Source locations over Etosha Pan for 2008–2011 determined using (a) LR2008 dust images. Source locations determined using (b) CSD images.

Broken down by year, we see that for both Etosha pan and the coastal regions the interannual variability in the percentage of plumes detected using LR2008 dust imagery mimics that seen in the percentage of dusty days detected. Since we never identify a dusty day in the LR2008 dust imagery which is not seen using the CSD method, this correlation suggests that in these regions on days identified as dusty by both rendering schemes the LR2008 dust scheme will identify the majority of individual plumes identified using the CSD technique. However, in the Makgadikgadi region it is apparent that although several distinct plumes identified by the CSD technique can combine to show a discernible signal in the LR2008 dust rendering this does not necessarily imply that they will be distinguishable and thus counted as separate plumes using the latter scheme. As can be seen from Case study I, multiple plumes from distinct sources within the region can be identified using the CSD technique: arguably each contributes to the signal observed in the LR2008 dust imagery and are thus said to be visible in this rendering. However, for this case only two distinct plumes and sources would be counted and located using the LR2008 dust imagery alone. For this reason even when the result of a dust emission is visible in the LR2008 dust rendering, fewer sources are identified. The significant difference in the plume success rate between the regions appears in part due to the fact that over Makgadikgadi there is, in general, more plumes seen per dusty day in the CSD imagery compared to the other regions.

In addition to reducing the number of distinct dust plumes counted, the diffuse nature of the signal seen in the LR2008 dust imagery also influences the precise dust source location that can be derived from these images. This problem is compounded by the fact that dust is often only visible in the LR2008 dust images sometime after initial activation is observed in the CSD images. For the 4 year period as a whole it was found the CSD technique offered a slight (1 or 2 h) to significant (3 h or more) advantage in providing earlier detection of events that were seen in both data sets. This behavior is consistent with the behavior seen in Case study I and shown in Figure 6.

Taken together, the differences in the number of dusty days detected and the number of individual plumes distinguished result in a significantly different picture of source locations obtained for this period using the

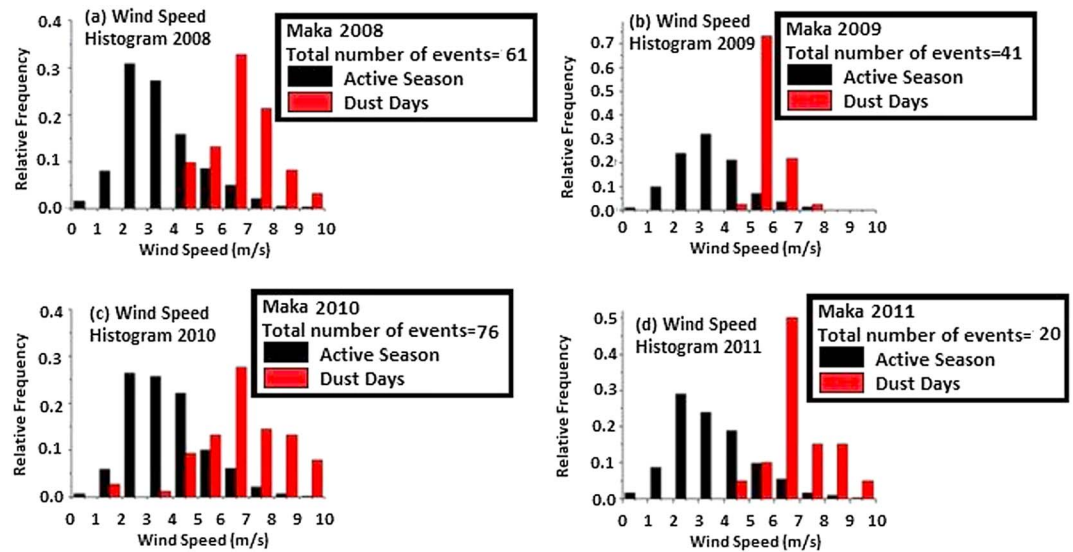


Figure 13. Black: Active dust emission season ERA-I wind speeds plotted as a function of relative wind speed frequency. Red: ERA-I wind speeds for dust days only as a function of relative wind speed frequency.

two different methods. As an example, Figure 12a shows all the plume source origins detected in this study for Etosha pan, differentiated by year and detection technique using LR2008 dust imagery, while Figure 11b shows the equivalent CSD plume source origins. The plume source locations defined using LR2008 dust imagery have a slight southwestward bias compared to the corresponding CSD defined locations. This can partly be explained by the fact that the dust events here are often associated with easterly to northeasterly winds (see, for example, Figure 10), and there is a tendency for later detection of plumes in LR2008 dust images (i.e., plumes in transit rather than at source) relative to the CSD imagery. It is possible to use air mass trajectory models to track the dust layer identified by the LR2008 dust images back to ground source, but this can be confounded if the “plume” is an amalgam originating from multiple unresolved sources. Figures 12a and 12b also demonstrates interannual variability in the locations of dust emission with a strong enhancement of plumes from eastern Etosha in 2010. This behavior is consistent with climatological factors controlling the emission and will be investigated in a forthcoming publication.

3.3.2. Meteorological Context for Dust Retrievals

For the purposes of this paper we check the fidelity of the CSD detected dust days by using ERA-I data (wind and wind gusts) to determine if the “dust events” were associated with sensible meteorological conditions. Previous work has demonstrated that events are associated with transient eddy activity [Eckardt *et al.*, 2001] which ERA-I resolves readily. Figure 13 shows the 2008–2011 ERA-I wind speeds, binned and plotted as relative frequencies, for the Makgadikgadi region. Dusty days, days on which dust plumes are observed emitted from the region of interest, are then binned according to the corresponding ERA-I wind speed for each dust day and plotted as a relative frequency on the same graph. Our observed dust emission days show a significant correlation with higher wind speeds, as might be expected, and typically peak at wind speeds of 6 m s^{-1} – 7 m s^{-1} .

To further evaluate our approach, ERA-I data also allow us to extract other components of the near-surface wind regime. In North Africa, Engelstaedter and Washington [2007a, 2007b] found improved agreement between ERA-40 wind gust data and dust source activity: attributed to the importance of turbulence and near surface convergence on dust uplift. Again, dusty days, days on which dust plumes are observed emitted from the region of interest using the CSD approach, were then evaluated according to the corresponding ERA-I wind gust data. As an example, Figure 14 provides a detailed summary of ERA-I surface gust data collected in the morning over Etosha Pan for two dust seasons with the highest and lowest event totals ($n=76$, 2010 and $n=20$, 2011). Again, for both years our observed dust emission days show significantly higher values for all extracted wind gust speed metrics (vertical profile, mean, maximum, and minimum). These data can also provide insights into the dust uplift mechanism at this location.

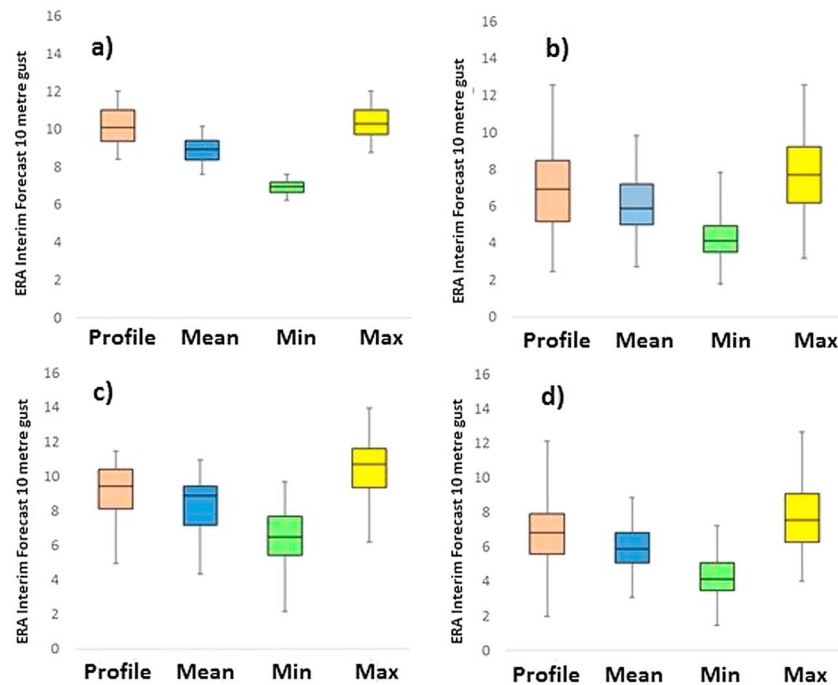


Figure 14. Box plots of Atmospheric Model 3 Surface ERA Interim Forecast 10 m wind gust data (morning) for Etosha Pan dust seasons in (a) CSD DSD 2010, (b) non-DSD 2010, (c) CSD DSD 2011, and (d) non-DSD 2011. In each case significant differences are apparent between profile, mean, minimum, and maximum wind gust values for observed CSD extracted dusty days (DSD) and nondusty days (non-DSD) [ERA-I, 2009].

4. Concluding Remarks

We have presented an image rendering method using SEVIRI narrowband channels, aimed at improving identification of dust source location and determining emission evolution over three key source regions in southern Africa. Enhancement of the dust signal in the rendered image is facilitated by subtraction of an estimated clear-sky composite signal from the observed reflectance and brightness temperatures. The algorithm employed to derive this clear-sky composite is relatively simple and can be readily applied to the large data sets associated with an imager in geostationary orbit that has high temporal and relatively high spatial resolution. In this work we used a single threshold and averaging period based on a short survey of the region designed to enhance the signals associated with the transient dust presence over both land and sea pixels. This represents a compromise, and improved plume contrast may be obtainable by further tuning of the thresholds and averaging window for specific applications and conditions. For example, at certain periods southern African land pixels show variable levels of surface moisture that result in a higher day-to-day variability in reflectance than that due to vegetation changes, examples of this can be seen for the Etosha pixel in Figure 2 and the Makgadikgadi pixel in Figure 3. Approaching and during the wet season reducing the averaging window would therefore be beneficial. Conversely, over coastal sea pixels the high frequency of cloud cover and ocean mist greatly reduces the number of clear-sky observations available for the composite average. Given the slow variation in ocean reflectance with time, the averaging window could be increased to improve the number of averaged clear-sky observations.

In enhancing the weaker transient signals we lose the dynamic range within the data set, and it therefore becomes more difficult to use this scheme as part of an automated detection routine as it relies on a degree of human interpretation of the patterns associated with dust emission. However, the use of this enhancement method does allow an informed observer to identify weak signals that may not be apparent in established imaging methods, and it can be easily tuned for a specific application and region to optimize its performance. This clear-sky differencing (CSD) technique also allows finer detail to be seen by removing the modulation of the signal by the underlying surface variation and greatly improves our ability to study dust source sites. Different combinations of channels have different sensitivities to dust presence at different times of day

and over different surface types and so add benefit to the detection process when used in conjunction with one another.

We have applied the CSD technique to the SEVIRI data set covering 2008 to 2011 in support of the DO4models project and compared dust detection and source location obtained from this imagery with the widely used dust imagery introduced by *Lensky and Rosenfeld* [2008, LR2008]. The results show that the advantages in detecting dust, distinguishing multiple sources and observing dust closer to time of activation and source location demonstrated by our technique for specific case study examples, are frequently manifested and consistent from year to year over all seasons and for a wide range of daylight hours. In addition to an improved ability to distinguish dust sources, our technique also detects a significant proportion of dust events not visible in the LR2008 imagery. Over the 4 years surveyed these advantages result in a significant difference in the dust events counted and the sources which are distinguished and result in the identification of activity and source regions not identified using the LR2008 thermal dust imagery alone. The survey also highlights how the specific detection method chosen can result in a markedly different picture of dust source locations and activity and thus is an important aspect to consider when developing a reliable climatology.

Using the approach we outline here, our intention is to exploit a more comprehensive data set to provide greater insight into the regional timing and precise location of dust events and hence the surface and meteorological factors controlling dust emission.

Acknowledgments

This work was carried out under the DO4Models Project. J. E. Murray was supported by NERC grant NE/H021450/1. The Terra MODIS level 1b data were acquired from the level-1 and Atmospheric Archive and Distribution System (LAADS) Distributed Active Archive Center (DAAC), located in the Goddard Space Flight Center in Greenbelt, Maryland (<https://ladsweb.nascom.nasa.gov/>). Access to CALIPSO data was obtained from the NASA Langley Research Center Atmospheric Science Data Center, https://eosweb.larc.nasa.gov/project/calipso/calipso_table. SEVIRI data courtesy of EUMETSAT's EUMETCAST dissemination mechanism, <http://www.eumetsat.int/website/home/Data/DataDelivery/EUMETCast/index.html>.

References

- Ackerman, S. A. (1989), Using the radiative temperature difference at 3.7 and 11 microns to track dust outbreaks, *Remote Sens. Environ.*, *27*, 129–133.
- Ackerman, S. A. (1997), Remote sensing aerosols using satellite infrared observations, *J. Geophys. Res.*, *102*, 17,069–17,079, doi:10.1029/96JD03066.
- Allen, C. J. T., R. Washington, and A. Saci (2015), Dust detection from ground based observations in the summer global dust maximum: Results from Fennec 2011 and 2012 and implications for modelling and field observations, *J. Geophys. Res. Atmos.*, *120*, 897–916, doi:10.1002/2014JD022655.
- Ashpole, I., and R. Washington (2013), A new high-resolution central and western Saharan summer time dust source map from automated satellite dust plume tracking, *J. Geophys. Res. Atmos.*, *118*, 6981–6995, doi:10.1002/jgrd.50554.
- Baddock, M. C., J. Bullard, and R. G. Bryant (2009), Dust source identification using MODIS: A comparison of techniques applied to the Lake Eyre Basin, Australia, *Remote Sens. Environ.*, *113*, 1511–1523.
- Banks, J. R., and H. E. Brindley (2013), Evaluation of MSG-SEVIRI mineral dust retrieval products over North Africa and the Middle East, *Remote Sens. Environ.*, *128*, 58–73, doi:10.1016/j.rse.2012.07.017.
- Bhattachan, A., P. D'Odorico, M. C. Baddock, T. M. Zobeck, G. S. Okin, and N. Cassar (2012), The Southern Kalahari: A potential new dust source in the Southern Hemisphere?, *Environ. Res. Lett.*, *7*, 024001.
- Bhattachan, A., P. D'Odorico, and G. S. Okin (2015), Biogeochemistry of dust sources in Southern Africa, *J. Arid Environ.*, doi:10.1016/j.jaridenv.2015.02.013.
- Brindley, H., P. Knippertz, C. Ryder, and I. Ashpole (2012), A critical evaluation of the ability of the Spinning Enhanced Visible and InfraRed Imager (SEVIRI) thermal infrared red-green-blue rendering to identify dust events: Theoretical analysis, *J. Geophys. Res.*, *117*, D07201, doi:10.1029/2011JD017326.
- Bryant, R. G. (2003), Monitoring hydrological controls on dust emissions: Preliminary observations from Etosha Pan, Namibia, *Geogr. J.*, *169*(2), 131–141, doi:10.1111/1475-4959.04977.
- Bryant, R. G. (2013), Recent advances in our understanding of dust source emission processes, *Prog. Phys. Geogr.*, *37*(3), 397–421, doi:10.1177/0309133313479391.
- Bryant, R. G., G. R. Bigg, N. M. Mahowald, F. D. Eckhardt, and S. G. Ross (2007), Dust emission response to climate in southern Africa, *J. Geophys. Res.*, *112*, D09207, doi:10.1029/2005JD007025.
- Cohen, J., P. Cohen, S. G. West, and L. S. Aiken (2003), *Applied Multiple Regression/Correlation Analysis for the Behavioral Sciences*, 3rd ed., Lawrence Erlbaum Assoc., Mahwah, N. J.
- Eckardt, F. D., R. Washington, and J. Wilkinson (2001), The origin of dust on the west coast of southern Africa, *Palaeoecol. Afr. Surrounding Isl.*, *27*, 207–219.
- Engelstaedter, S., and R. Washington (2007a), Atmospheric controls on the annual cycle of North African dust, *J. Geophys. Res.*, *112*, D03103, doi:10.1029/2006JD007195.
- Engelstaedter, S., and R. Washington (2007b), Temporal controls on global dust emissions: The role of surface gustiness, *Geophys. Res. Lett.*, *34*, L15805, doi:10.1029/2007GL029971.
- ERA-I (2009), European Centre for Medium-Range Weather Forecasts. 2009, updated monthly, ERA-Interim Project, Res. Data Arch. at the Natl. Cent. for Atmos. Res., Comput. and Inf. Syst. Lab., doi:10.5065/D6CR5RD9.
- Ginoux, P., J. M. Prospero, T. E. Gill, N. C. Hsu, and M. Zhao (2012), Global-scale attribution of anthropogenic and natural dust sources and their emission rates based on MODIS Deep Blue aerosol products, *Rev. Geophys.*, *50*, RG3005, doi:10.1029/2012RG000388.
- Goudie, A., and H. Viles (2015), Etosha Pan and the Karstveld, in *Landscapes and Landforms of Namibia*, pp. 61–65, Springer, Dordrecht, Netherlands.
- Haustein, K., R. Washington, J. King, G. Wiggs, D. S. G. Thomas, F. D. Eckardt, R. G. Bryant, and L. Menut (2015), Testing the performance of state-of-the-art dust emission schemes using DO4Models field data, *Geosci. Model Dev.*, *8*, 341–362.
- Ipe, A., N. Clerbaux, C. Bertrand, S. Dewitte, and Gonzalez, L. (2003), Pixel-scale composite top-of-the-atmosphere clear-sky reflectances for Meteosat-7 visible data, *J. Geophys. Res.*, *108*(D19), 4612, doi:10.1029/2002JD002771.
- Lensky, I. M., and D. Rosenfeld (2008), Clouds-Aerosols-Precipitation Satellite Analysis Tool (CAPSAT), *Atmos. Chem. Phys.*, *8*, 6739–6753.

- Marchese, F., M. Ciampa, C. Filizzola, T. Lacava, G. Mazzeo, N. Pergola, and V. Tramutoli (2010), On the exportability of Robust Satellite Techniques (RST) for active volcano monitoring, *Remote Sens.*, *2*, 1575–1588, doi:10.3390/rs2061575.
- Matthews, E., and W. B. Rossow (1987), Regional and seasonal variations of surface reflectances from satellite observations at 0.6 μm , *J. Climate Appl. Meteorol.*, *26*, 170–202.
- Miller, S. D. (2014), System and method for atmospheric parameter enhancement, United States Patent Application Publication, Pub no. US 2014/0212061 A1.
- Minnis, P., and E. F. Harrison (1984), Diurnal variability of regional cloud and clear-sky radiative parameters derived from GOES data. Part I: Analysis method, *J. Climate Appl. Meteorol.*, *23*, 993–1011.
- MODIS Characterisation Support Team (2006), MODIS Level-1B Product User's Guide, MCST Document PUB-01-U-0202- Rev B. Release. [Available at mcst.gsfc.nasa.gov/sites/mcst.gsfc/files/file_attachments/M1054.pdf.]
- Myhre, G., T. Berntsen, J. Haywood, J. Sundet, B. Holben, M. Johnson, and F. Stordal (2003), Modeling the solar radiative impact of aerosols from biomass burning during the Southern African Regional Science Initiative (SAFARI-2000) experiment, *J. Geophys. Res.*, *108*(D13), 8501, doi:10.1029/2002JD002313.
- Piketh, S. J., P. D. Tyson, and S. Steffen (2000), Aeolian transport from southern Africa and iron fertilization of marine biota in the South Indian Ocean, *S. Afr. J. Sci.*, *96*, 244–246.
- Piketh, S. J., R. J. Swap, W. Maenhaut, H. J. Annegarn, and P. Formenti (2002), Chemical evidence of long-range atmospheric transport over southern Africa, *J. Geophys. Res.*, *107*(D24), 4817, doi:10.1029/2002JD002056.
- Prospero, J. M., P. Ginoux, O. Torres, S. E. Nicholson, and T. E. Gill (2002), Environmental characterization of global sources of atmospheric soil dust derived from Nimbus-7 TOMS absorbing aerosol product, *Rev. Geophys.*, *40*(1), 1002, doi:10.1029/2000RG000095.
- Puschell, J. J., H. A. Lowe, J. Jeter, S. Kus, W. T. Hurt, D. Gilman, D. Rogers, and R. Hoelzer (2002), Japanese Advanced Meteorological Imager: A next generation GEO imager for MTSAT-1R, in *Proceedings of the SPIE-Earth Observing Systems VII*, vol. 4814, pp. 152–161, doi:10.1117/12.453755.
- Puschell, J. J., et al. (2006), In-flight performance of the Japanese Advanced Meteorological Imager, *SPIE Proc.*, *6296*, 62960N, doi:10.1117/12.683505.
- Rossow, W. B., and L. C. Garder (1993), Cloud detection using satellite measurements of infrared and visible radiances for ISCCP, *J. Clim.*, *6*, 2341–2369.
- Schepanski, K., I. Tegen, B. Laurent, B. Heinold, and A. Macke (2007), A new Saharan dust source activation frequency map derived from MSG-SEVIRI IR-channels, *Geophys. Res. Lett.*, *34*, L18803, doi:10.1029/2007GL030168.
- Schepanski, K., I. Tegen, M. C. Todd, B. Heinold, G. Bonisch, B. Laurent, and A. Macke (2009), Meteorological processes forcing Saharan dust emission inferred from MSG-SEVIRI observations of subdaily dust source activation and numerical models, *J. Geophys. Res.*, *114*, D10201, doi:10.1029/2008JD010325.
- Schepanski, K., I. Tegen, and A. Macke (2012), Comparison of satellite based observations of Saharan dust source areas, *Remote Sens. Environ.*, *123*, 90–97.
- Schmetz, J., P. Pili, S. Tjemkes, D. Just, J. Kerkmann, S. Rota, and A. Ratier (2002), An introduction to Meteosat Second Generation (MSG), *Bull. Am. Meteorol. Soc.*, *83*, 977–992.
- Tjemkes, S. A. (2005), On the conversion from radiances to equivalent brightness temperatures. [Available at http://www.eumetsat.int/groups/ops/documents/document/pdf_msg_seviri_rad2bright.pdf.]
- Tramutoli, V. (2007), Robust Satellite Techniques (RST) for natural and environmental hazards monitoring and mitigation: Theory and applications, in *Proceedings of Multitemp 2007*, pp. 1–6, IEEE, doi:10.1109/MULTITEMP.2007.4293057.
- Tramutoli, V., C. Filizzola, F. Marchese, G. Mazzeo, R. Paciello, N. Pergola, C. Pietrapertosa, and F. Sannazzaro (2010), A Robust Satellite Technique (RST) for dust storm detection and monitoring: The case of 2009 Australian event, in *Proceedings of the 2010 IEEE International Geoscience and Remote Sensing Symposium, Honolulu, Hawaii, 25–30 July 2010*, pp. 1707–1709, doi:10.1109/IGARSS.2010.5650621.
- Tummon, F., F. Solomon, C. Lioussé, and M. Tadross (2010), Simulation of the direct and semi-direct aerosol effects on the southern Africa regional climate during the biomass burning season, *J. Geophys. Res.*, *115*, D19206, doi:10.1029/2009JD013738.
- Vickery, K., F. D. Eckardt, and R. G. Bryant (2013), A sub-basin scale dust plume source frequency inventory for southern Africa, 2005–2008, *Geophys. Res. Lett.*, *40*, 5274–5279, doi:10.1002/grl.50968.
- Wald, A., Y. Kaufmann, D. Tanre, and B.-C. Gao (1998), Daytime and nighttime detection of mineral dust over desert using infrared spectral contrast, *J. Geophys. Res.*, *103*, 32,307–32,313, doi:10.1029/98JD01454.
- Washington, R., M. Todd, N. J. Middleton, and A. S. Goudie (2003), Duststorm areas determined by the Total Ozone Monitoring Spectrometer and surface observations, *Ann. Assoc. Am. Geogr.*, *93*, 297–313.
- Williams, C. A. (2010), Integration of remote sensing and modelling to understand carbon fluxes and climate interactions in Africa, in *Ecosystem Function in Global Savannas: Measurement and Modelling at Landscape to Global Scales*, edited by M. J. Hill and N. P. Hanan, CRC Press, Boca Raton, Fla.
- Zhang, Y., et al. (2015), Modeling the global emission, transport and deposition of trace elements associated with mineral dust, *Biogeosciences*, *12*(19), 5771–5792.